

Possibility for survival of macroscopic turbulence in porous media with high porosity

Feixiong Rao^{1,†} and Yan Jin^{1,2}

¹Center of Applied Space Technology and Microgravity (ZARM), University of Bremen, 28359 Bremen, Germany

²MAPEX Center for Materials and Processes, University of Bremen, 28359 Bremen, Germany

(Received 19 February 2021; revised 14 October 2021; accepted 24 January 2022)

The direct numerical simulation (DNS) study by Jin *et al.* (*J. Fluid Mech.*, vol. **766**, 2015, pp. 76–103) shows that the turbulent structures are generally restricted in size to the pore scale, leading to the pore-scale prevalence hypothesis (PSPH). Although the PSPH has been validated under most conditions, it might become invalid as the porosity approaches unity. In order to investigate the valid domain of the PSPH, we have studied the turbulent flows in porous matrices which have one or two length scales using DNS and macroscopic simulation methods. The large porous elements are made of staggered arrays of square cylinders, which might stimulate strong macroscopic (large-scale) turbulence. The small porous elements are made of aligned arrays of spheres or cubes, which suppress the macroscopic turbulence. The analyses are performed for various values of the Reynolds number, Darcy number, pore-scale ratio and porosity. Turbulent two-point correlations, integral length scales and premultiplied energy spectra are calculated from the DNS and macroscopic simulation results to determine the length scale of the turbulent structures. Our numerical results show that the flow becomes turbulent when the Reynolds number is sufficiently large. However, the length scale of turbulence is not considerably affected by the Reynolds number, Darcy number and pore-scale geometry. The PSPH is valid when the porosity has small or medium values. At a sufficiently large Reynolds number, large-scale turbulence survives if the porosity is larger than a critical value. Our DNS and macroscopic simulation results show that this critical value is in the range 0.93–0.98 for porous matrices with large Darcy numbers (0.3–1.26 using the definition in this study). The dependence of the critical porosity on the pore-scale geometry still needs to be further investigated.

Key words: viscoelasticity, microfluidics

† Email address for correspondence: feixiong.rao@zarm.uni-bremen.de

© The Author(s), 2022. Published by Cambridge University Press. This is an Open Access article, distributed under the terms of the Creative Commons Attribution licence (<https://creativecommons.org/licenses/by/4.0/>), which permits unrestricted re-use, distribution, and reproduction in any medium, provided the original work is properly cited.

1. Introduction

A porous medium refers to a material consisting of a solid matrix with interconnected voids. Flows in porous media are often laminar due to the low Reynolds number. However, at certain conditions, the Reynolds number based on the pore scale might exceed its critical value for laminar–turbulence transition and thus the flow becomes turbulent.

Turbulence in porous media can be often found in canopy flows. The examples include the flows in porous canopies made of trees, vegetation or buildings (Meroney 2007). These canopies usually have large porosities (typically >90%, see Ghisalberti & Nepf (2009)) and high permeability (10^{-4} – 10^{-1} m², see Rubol, Ling & Battiato (2018)). Whether macroscopic turbulence can survive or not in porous media is a significant question for these applications. It might enhance pollutant removal in wetland (Serra, Fernando & Rodriguez 2004), benefit vegetation by augmenting nutrient uptake and/or gas exchange (Nepf 2012), influence biological and ecological mechanisms (de Langre 2008) and help to blow air pollutants in a city away efficiently. One type of macroscopic turbulence is generated due to Kelvin–Helmholtz stability which occurs at the canopy interface. Many studies about this type of macroscopic turbulence can be found, see Breugem, Boersma & Uittenbogaard (2006), Suga (2016), Kim *et al.* (2020) as examples. Nepf (2012) indicated that the lower canopy, which is far below the interface, is associated with pore-scale turbulence. However, when the lower canopy has more than one length scale, the large-scale turbulence stimulated by the large porous elements (e.g. tree trunks in a forest canopy) can be also treated as macroscopic turbulence. This macroscopic turbulence might survive if it cannot be suppressed by the small porous elements (e.g. tree leaves, stems or grasses).

Possibility for survival of macroscopic turbulence in porous media has been intensively studied in past years. There are two distinct views on this question. According to the first view, macroscopic turbulence in porous media is believed to be possible, see Lee & Howell (1991) and Antohe & Lage (1997). Transport of turbulence kinetic energy should be accounted for when there is macroscopic turbulence. The examples include the models by Prescott & Incropera (1995), Antohe & Lage (1997), Getachew, Minkowycy & Lage (2000) and de Lemos (2012). Macroscopic turbulence models have also been used to simulate flow in a porous matrix represented by a periodic array of square cylinders (Kazerooni & Hannani 2009; Kundu, Kumar & Mishra 2014). Belcher, Harman & Finnigan (2012) suggested that canopy flows are characterized by the drag length scale rather than the depth of the canopy. However, it is not clear if the drag length scale is related to macroscopic turbulence.

In the second view, macroscopic turbulence is impossible because of the limitation on the size of turbulent eddies imposed by the pore scale, see Nield (1991, 2001), Nakayama & Kuwahara (1999) and Kuwahara *et al.* (1998) as examples. Using an experimental method, Tanino & Nepf (2008) suggested that the integral length scale of turbulence is determined by the minimum value of the surface-to-surface distance between cylinders and the cylinder diameter, both of which belong to pore scales. They further proposed that only turbulent eddies with mixing length scales greater than the cylinder diameter contribute significantly to dispersion, which is the transport of solute due to both time fluctuations and spatial deviations of microscopic velocity and species concentration. Through a direct numerical simulation (DNS) study of turbulent flows in a porous medium made of square cylinders, Jin *et al.* (2015) concluded the turbulent eddies are generally restricted by the pore size, leading to the pore-scale prevalence hypothesis (PSPH). Uth *et al.* (2016) and Jin & Kuznetsov (2017) confirmed the PSPH with the DNS results for different geometries

of the porous matrix. Rao, Kuznetsov & Jin (2020) developed a macroscopic model based on the PSPH, in which microscopic turbulence is modelled.

However, the PSPH has a boundary of validity. If the porosity approaches unity, the effect of the porous matrix on the flow will disappear. Macroscopic turbulence will survive under such a condition. In Uth *et al.* (2016), a second (large) element is imposed in the porous matrix; it can stimulate strong large-scale turbulence. The DNS results show that, when the porosity for the porous matrix made of small length scales is large enough, the macroscopic turbulence seems to survive. Chu, Weigand & Vaikuntanathan (2018) and Srikanth *et al.* (2018) also confirmed the existence of large turbulent structures for flows with large porosities. Therefore, the PSPH should have a boundary of validity, out of which macroscopic turbulence might survive.

The purpose of this study is to find out in what conditions the large turbulent structures might survive. To achieve this goal, the turbulent flows in a porous matrix with two length scales will be calculated by using both DNS and macroscopic simulation methods. Strong large-scale turbulence can be stimulated by the large porous matrix. The spacing between small porous elements is varied to obtain different porosity values. The PSPH macroscopic model proposed by Rao *et al.* (2020) will be used in the macroscopic simulation. While the microscopic turbulence is modelled in the PSPH model, it is possible to resolve the macroscopic turbulence directly when it can survive. The DNS and macroscopic simulation results will verify and complement each other in the study.

2. Geometry of the porous matrix

The porous matrix in this study is made of two-dimensional staggered arrays of bars with the element size d_l and spacing s_l and three-dimensional aligned arrays of spheres or cubes with the element size d_s and spacing s_s , see figure 1(a,b). The computational domain is a representative elementary volume (REV) for the large porous element. The ratio between the large pore size s_l and the bar size d_l has a fixed value ($s_l/d_l = 2$). The same domain size ($2s_l \times 2s_l \times s_l$) is used for all test cases.

The porous matrices are made of the same large porous elements (staggered bars) but different numbers of REV's have been studied in Jin *et al.* (2015). The numerical results show that the computational domain in this study is large enough to calculate the length scale of turbulence at the centre of a REV accurately.

The flow is in x_1 direction. The Reynolds numbers for the large and small elements are defined as

$$Re_s = \frac{u_m d_s}{\nu}, \quad Re_l = \frac{u_m d_l}{\nu}, \quad (2.1a,b)$$

where u_m is the mean seepage velocity.

The Reynolds number Re_K for a generic porous matrix (GPM) made of small porous elements can be defined as

$$Re_K = \frac{u_m \sqrt{K}}{\nu}, \quad (2.2)$$

where K is the permeability. The Darcy number Da for the GPM is defined as

$$Da = K/d_l^2, \quad (2.3)$$

ϕ_s denotes the porosity for the porous matrix made of small porous elements. For the porous matrix made of spheres, ϕ_s is calculated as

$$\phi_s = 1 - \frac{\pi}{6} \left(\frac{d_s}{s_s} \right)^3. \quad (2.4)$$

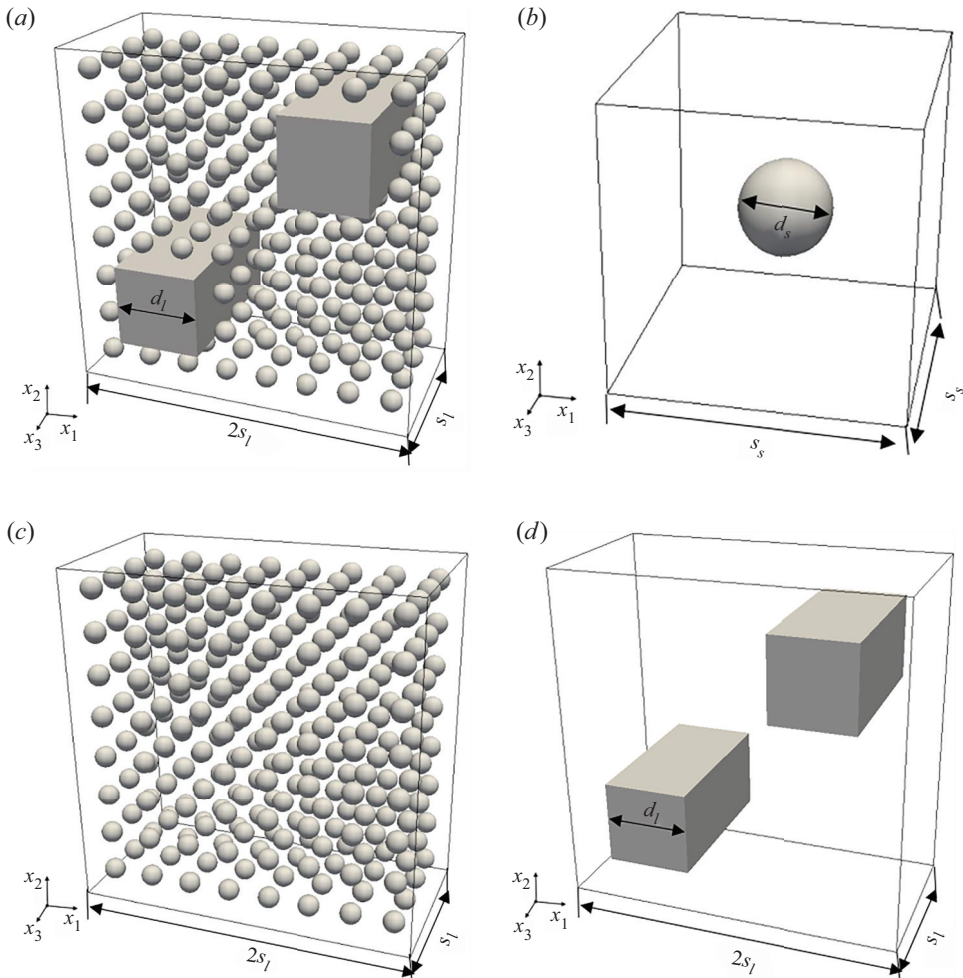


Figure 1. Porous matrices used in the study. (a) A porous matrix with two length scales (made of cubes and spheres); (b) a REV for the small porous element; (c) a porous matrix with only small pore scale (made of spheres); (d) a porous matrix with only large pore scale (made of bars).

For the porous matrix made of cubes, ϕ_s is calculated as

$$\phi_s = 1 - \left(\frac{d_s}{s_s}\right)^3. \tag{2.5}$$

In order to make the comparison, we have also calculated the flows in porous matrices with only one length scale. They are made of either only large porous elements (figure 1c) or only small porous elements (figure 1d).

3. Governing equations and numerical methods

3.1. DNS

In DNS, the transient Navier–Stokes equations accounting for all scales of turbulent motions are solved directly without using any turbulence model. For flows in porous

media, the detailed pore-scale geometry is also resolved. The governing equations for an incompressible flow read

$$\frac{\partial u_i}{\partial x_i} = 0, \tag{3.1}$$

$$\frac{\partial u_i}{\partial t} + \frac{\partial u_i u_j}{\partial x_j} = -\frac{\partial p}{\partial x_i} + \nu \frac{\partial^2 u_i}{\partial x_j^2} + g_i, \tag{3.2}$$

where g_i is the applied pressure gradient in the momentum equation which maintains a constant flow rate. A set of general units (L for length and T for time) are used in the study so that the numerical results can be applied in any system of units.

The governing equations (3.1)–(3.2) are solved by using a lattice-Boltzmann method (LBM). The basic equation for the present LBM is a discretized version of the Boltzmann equation (Aidun & Clausen 2009). The collision operator is modelled by the Bhatnagar–Gross–Krook (BGK) model (Bhatnagar, Gross & Krook 1954),

$$f_i(\mathbf{x} + \boldsymbol{\xi}_i \Delta t, t + \Delta t) - f_i(\mathbf{x}, t) = -\frac{1}{\tau} (f_i(\mathbf{x}, t) - f_i^{eq}(\mathbf{x}, t)), \tag{3.3}$$

where $\boldsymbol{\xi}_i$ is a discrete particle velocity, $f_i(\mathbf{x}, t)$ is the number distribution of molecules at a position \mathbf{x} at a time t along with direction i , $f_i^{eq}(\mathbf{x}, t)$ is the equilibrium form of $f_i(\mathbf{x}, t)$ and τ is the relaxation time which determines the kinematic viscosity (see Chen & Doolen 1998).

With the help of the Chapman–Enskog expansion (see Chen & Doolen 1998), (3.3) solves the incompressible Navier–Stokes equations (3.1)–(3.2) by streaming and collision processes. The left-hand side term represents the streaming process while the right-hand side term represents the collision process. Equation (3.3) is a linear partial differential equation and the meshes are uniformly distributed in all directions, which leads the LBM to run efficiently on massively parallel architectures. The bounce-back model with numerical approximation of second order is applied to the wall surfaces of the porous elements. More details can be found in Mohamad (2011).

3.2. Macroscopic simulation

Direct numerical simulation is the most accurate method for studying turbulent flows in porous media, however, it is extremely expensive, particular for porous media with high porosities and low Darcy numbers. So, some cases are calculated by using macroscopic simulation. Some DNS cases are calculated again using the macroscopic simulation solver for validation.

The large porous elements (bars) are still fully resolved in macroscopic simulation while the small porous elements are modelled. Volume averaging (3.1)–(3.2) in each REV and using the theorem of local volumetric average (Slattery 1967; Whitaker 1969, 1999; Gray & Lee 1977), the macroscopic equations for flows in a porous medium can be obtained, expressed as

$$\frac{\partial u_{Di}}{\partial x_i} = 0, \tag{3.4}$$

$$\frac{\partial u_{Di}}{\partial t} + \frac{\partial (u_{Di} u_{Di} / \phi)}{\partial x_j} = -\frac{\partial (\phi \langle p \rangle^i)}{\partial x_i} + \phi g_i - \phi R_i + \nu \frac{\partial^2 u_{Di}}{\partial x_j^2} - \frac{\partial (\phi \langle u_i^i u_j^j \rangle^i)}{\partial x_j}. \tag{3.5}$$

The operator $\langle \cdot \rangle^i$ denotes volume averaging over the fluid region of an REV. Here $u_{Di} = \phi \langle u_i \rangle^i$ is the superficial velocity and R_i denotes the total drag caused by the effect of the porous matrix. The spatial deviation ${}^i u_i$ is the difference between the value at a point and its intrinsic average, calculated as ${}^i u_i = u_i - \langle u_i \rangle^i$.

Rao *et al.* (2020) assumed in the PSPH model that macroscopic turbulence does not exist when the porosity is not very large, so only microscopic turbulence is accounted for in this model. However, it is still possible to capture the macroscopic turbulence directly using this model if it survives. Now R_i is decomposed into a drag term R_i^* which is determined by u_{Di} and the residual drag term $R_i - R_i^*$ related to the gradient of u_{Di} . Making a Taylor extension for R_i^* with respect to a local Reynolds number $Re_K = \sqrt{K}|u_D|/\nu$ and taking the first two leading-order terms, we have

$$R_i^* = \frac{\nu}{K} u_{Di} (1 + c_{F1} Re_K). \tag{3.6}$$

Equation (3.6) is identical to the Forchheimer extension of the Darcy term (Lage & Antohe 2000). For the small porous elements under consideration (aligned spheres or cubes), the Forchheimer coefficient c_{F1} is set to 0.1, see Nield & Bejan (2017) and Rao *et al.* (2020).

The sum of the momentum dispersion $\phi \langle {}^i u_i {}^j u_j \rangle^i$, molecular diffusion $2\nu s_{Dij}$ and drag due to the velocity gradient $R_i - R_i^*$ is modelled using a Laplacian term L_i , expressed as

$$L_i = \phi (R_i - R_i^*) + \nu \frac{\partial^2 u_{Di}}{\partial x_j^2} - \frac{\partial (\phi \langle {}^i u_i {}^j u_j \rangle^i)}{\partial x_j} = \frac{\partial}{\partial x_j} (2\tilde{\nu} s_{Dij}), \tag{3.7}$$

where $\tilde{\nu}$ is an effective viscosity. Rao *et al.* (2020) introduced another local Reynolds number to model the effective viscosity $\tilde{\nu}$, defined as

$$Re_d = \frac{K|s_D|}{\nu}, \tag{3.8}$$

where s_D is the strain rate tensor of the superficial velocity u_D . Making a Taylor expansion with respect to Re_d for $\tilde{\nu}/\nu$ and taking the first two leading-order terms, we have

$$\tilde{\nu}/\nu = c_{B1} + c_{B2} Re_d. \tag{3.9}$$

The model coefficients K , c_{F1} , c_{B1} and c_{B2} are all geometric parameters which are independent of the flow condition. They are determined empirically in this study. The permeability K can be approximated by the Carman–Kozeny equation (Kozeny 1927; Carman 1956), expressed as

$$K = \frac{D_{P2}^2 \phi^3}{c_K (1 - \phi)^2}, \tag{3.10}$$

where D_{P2} is an effective average particle or fibre diameter. The model coefficient c_K has the value 180, and c_{B1} and c_{B2} are calculated using the correlations in Rao *et al.* (2020),

they are

$$c_{B1} = 49.63 \times \frac{(1 - \phi)^2}{\phi^{0.5}} + 1, \quad (3.11)$$

$$c_{B2} = 0.79 \times \frac{(1 - \phi)^2}{\phi^3}. \quad (3.12)$$

Substituting (3.6) and (3.7) into (3.5), normalizing with the mean velocity u_m and the large element size d_l , the following dimensionless macroscopic equations can be obtained:

$$\frac{\partial \tilde{u}_{Di}}{\partial \tilde{x}_i} = 0, \quad (3.13)$$

$$\frac{\partial \tilde{u}_{Di}}{\partial \tilde{t}} + \frac{\partial (\tilde{u}_{Di} \tilde{u}_{Di} / \phi)}{\partial \tilde{x}_j} = - \frac{\partial (\phi \langle \tilde{p} \rangle^i)}{\partial \tilde{x}_i} + \phi \tilde{g}_i - \tilde{R}_i + \tilde{L}_i, \quad (3.14)$$

where \sim denotes a dimensionless variable. The dimensionless drag and Laplacian terms are calculated as

$$\tilde{R}_i = \frac{\phi}{Da Re_l} \tilde{u}_{Di} + \frac{\phi c_{F1}}{Da^{1/2}} |\tilde{\mathbf{u}}_D| \tilde{u}_{Di}, \quad (3.15)$$

$$\tilde{L}_i = 2 \frac{\partial}{\partial \tilde{x}_j} \left[\left(\frac{c_{B1}}{Re_l} + c_{B2} Da |\tilde{s}_D| \right) \hat{s}_{Dij} \right]. \quad (3.16)$$

When Re_l is high enough ($Re_l \rightarrow \infty$), (3.15) and (3.16) can be simplified as

$$\tilde{R}_i = \frac{\phi c_{F1}}{Da^{1/2}} |\tilde{\mathbf{u}}_D| \tilde{u}_{Di}, \quad (3.17)$$

$$\tilde{L}_i = \frac{\partial}{\partial \tilde{x}_j} (2c_{B2} Da |\tilde{s}_D| \tilde{s}_{Dij}). \quad (3.18)$$

Equation (3.17) is consistent with the momentum equation for canopy flows (Nepf 2012) in which the viscous resistance is neglected. It can be seen that the momentum transport is affected by the geometric parameters ϕ , c_{F1} , c_{B2} and Da when Re_l is high enough. If the correlations and model coefficients for calculating c_{B2} and the Forchheimer term are generic for all porous matrices, (3.13)–(3.14) are determined only by Da and ϕ . So, for a given value of Da , there is a critical value of porosity ϕ_c above which the macroscopic turbulence might occur.

A finite volume method (FVM) is used to solve the governing equations. The computational fluid dynamics (CFD) solver is developed based on the open source CFD program OpenFoam 18.06. The solutions are advanced in time, with the second-order implicit backward method. To compute the derivatives of the velocity, the variables at the interfaces of the grid cells are obtained using linear interpolation. The linear interpolation of the interfacial values leads to a second-order central difference scheme for spatial discretization. The pressure at the new time level is determined by the Poisson equation. The velocity is corrected with the pressure implicit with splitting of operators pressure velocity coupling scheme.

Porous matrix	ϕ_s	s_l/s_s	Mesh resolution	Re_s	Re_l
'bars+spheres'	0.61–0.98	4–12	353 × 353 × 177 1153 × 1153 × 577	355–704	781–4224
'bars+cubes'	0.88–0.98	4	641 × 641 × 321 1281 × 1281 × 641	614–749	2512–5992
'spheres'	0.61–0.98	—	353 × 353 × 177 961 × 961 × 481	391–754	860–4524
'cubes'	0.88–0.96	—	641 × 641 × 321 961 × 961 × 481	469–689	2352–4137
'bars'	1.0	—	161 × 161 × 81 201 × 201 × 201	—	528–653

Table 1. Main parameters for the DNS cases, LBM. The lowest and highest mesh resolutions for each porous matrix are shown.

Porous matrix	ϕ_s	s_l/s_s	Da	Mesh resolution	Re_K	Re_l
'bars+spheres'	0.93–0.99	4, 8	0.07–1.26	161 × 161 × 81	39–2009	62–5392
'bars+GPM'	0.93–0.99	—	0.3–1.2	161 × 161 × 81 256 × 256 × 256	∞	∞
'bars'	1.0	—	—	81 × 81 × 81 161 × 161 × 161	—	566–671

Table 2. Main parameters for the cases of macroscopic simulation, FVM. The lowest and highest mesh resolutions for each porous matrix are shown.

4. Results and discussion

4.1. Description of the test cases

The main parameters for DNS cases and macroscopic simulation cases are shown in [tables 1](#) and [2](#), respectively. The length scale ratio s_s/d_s is varied in the DNS cases to obtain the porosity values from 0.61 to 0.98. For $\phi_s = 0.7$, the pore-size ratio s_l/s_s varies between 4 and 12. Relatively large Reynolds numbers are studied ($Re_s > 350$ and $Re_l > 500$) to ensure the flows are in the fully turbulent regime; the laminar–turbulent transition is not in the scope of this study. The grid points are uniformly distributed in the DNS cases. Body fitted meshes are used in the cases of macroscopic simulation. A higher resolution mesh is used for flows with a higher Reynolds number, see [table 1](#) for the highest and lowest mesh resolutions for each geometry.

The effect of small porous elements is approximated using a continuous model in the macroscopic simulation. The geometric parameters are determined empirically, see details in [§ 3.2](#). The solid matrix geometry in the first group of test cases is assumed to be the same as 'bars+spheres' in DNS. The values of s_l/s_s are set to 4 and 8 so the macroscopic simulation results can be compared with the DNS results. In another group of cases, we have carried out the macroscopic simulation for $Re_l \rightarrow \infty$ to exclude the effect of the Reynolds number. The small porous elements are not specified in these cases and the Darcy number is given directly, so this porous matrix is called 'bars+GPM'. Equations (3.13) and (3.14) with the drag terms expressed by (3.17) and (3.18) are solved for the calculation of this group of cases.

Typical DNS and macroscopic simulation cases are calculated using two mesh resolutions to perform the mesh-convergence study. In addition, typical macroscopic

simulation results are compared with the DNS results for validation. Details about verification and validation are presented in the Appendix.

4.2. DNS results

The Q -method (Hunt, Wary & Moin 1988) is used to identify the turbulent structures in porous media qualitatively. The quantity $Q = -\frac{1}{2}(\partial u_i/\partial x_j)(\partial u_j/\partial x_i)$ is the second invariant of the instantaneous velocity gradient tensor. According to the Q -method, vortices can be identified by connected fluid regions with positive Q values. Figure 2 shows the turbulent structures identified by the isosurfaces of Q in different porous matrices. When the porous matrix has only large elements (staggered arrays of square cylinders), it can be seen in figure 2(a) that the size of vortices is close to the large pore size s_l .

For the porous matrix with only small porous elements, fully developed turbulence can be found when Re_s is approximately 500. The size of vortices is close to the small pore size s_s , which is much smaller than s_l , see figure 2(b).

If we combine the two porous elements together, we may investigate whether (or in what conditions) the vortices with the large length scale s_l may survive. The values of Re_s for the cases in figures 2(c) and 2(d) are still above 500. The size of turbulent structures is generally close to the small pore size s_s when the porosity has a medium value ($\phi_s = 0.7$), see figure 2(c). The vortical tubes are more densely populated in the passage between the two large porous elements. However, we have not observed any vortices which are evidently larger than s_s . All large vortices are damped by the porous medium made of small porous elements and vanish. This is in accordance with the PSPH. However, when the porosity is increased to $\phi_s = 0.98$, some vortical bulks which are much larger than s_s (close to the large element size d_l) can be found; their locations are indicated by the circles in figure 2(d). We can also see the long wakes downstream of the large vortical bulks. The vortical structures show qualitatively that the large-scale turbulence survives when $\phi_s = 0.98$.

However, the Q -method should be combined with other statistical results to perform quantitative analysis. In order to detect the length scale of turbulence quantitatively, the two-point correlation due to turbulence $\hat{R}_{ij}(\mathbf{r}, \mathbf{x}_0)$ is calculated. The correlation point \mathbf{x}_0 is at the centre of the cross-plane (s_l, s_l, x_3) . When the velocity components $u'_i(\mathbf{x}_0, t)$ and $u'_j(\mathbf{x}_0 + \mathbf{r}, t)$ are correlated, the overall two-point correlation $R_{ij}(\mathbf{r}, \mathbf{x}_0)$ can be directly calculated from the DNS results, it is defined as

$$R_{ij}(\mathbf{r}, \mathbf{x}_0) = \langle u'_i(\mathbf{x}_0, t)u'_j(\mathbf{x}_0 + \mathbf{r}, t) \rangle_t, \quad (4.1)$$

where the operator $\langle \cdot \rangle_t$ denotes the time averaging. To extract the correlation due to non-turbulent fluctuation from $R_{ij}(\mathbf{r}, \mathbf{x}_0)$ and calculate the correlation due to true turbulence $\hat{R}_{ij}(\mathbf{r}, \mathbf{x}_0)$, a lateral correlation is calculated as

$$\tilde{R}_{ij}(\mathbf{r}, r_3, \mathbf{x}_0) = \langle u'_i(\mathbf{x}_0, t)u'_j(\mathbf{x}_0 + \mathbf{r} + r_3\mathbf{e}_3, t) \rangle_t, \quad (4.2)$$

where \mathbf{e}_3 is the unit vector in the spanwise direction and r_3 is the value of distance. Due to the periodicity of the flow in the x_3 direction, we expect the non-turbulent correlation $\tilde{R}_{ij}(\mathbf{r}, \mathbf{x}_0)$ can be approximated by $\tilde{R}_{ij}(\mathbf{r}, r_3, \mathbf{x}_0)$ if r_3 is large enough. Thus, the turbulent two-point correlation can be calculated as

$$\hat{R}_{ij}(\mathbf{r}, \mathbf{x}_0) = R_{ij}(\mathbf{r}, \mathbf{x}_0) - \tilde{R}_{ij}(\mathbf{r}, r_3, \mathbf{x}_0). \quad (4.3)$$

The distributions of $\hat{R}_{11}(\mathbf{r}, \mathbf{x}_0)$ for turbulent flows in porous matrices with two length scales ('bars+spheres') or only one length scale ('bars' or 'spheres') are shown in figure 3.

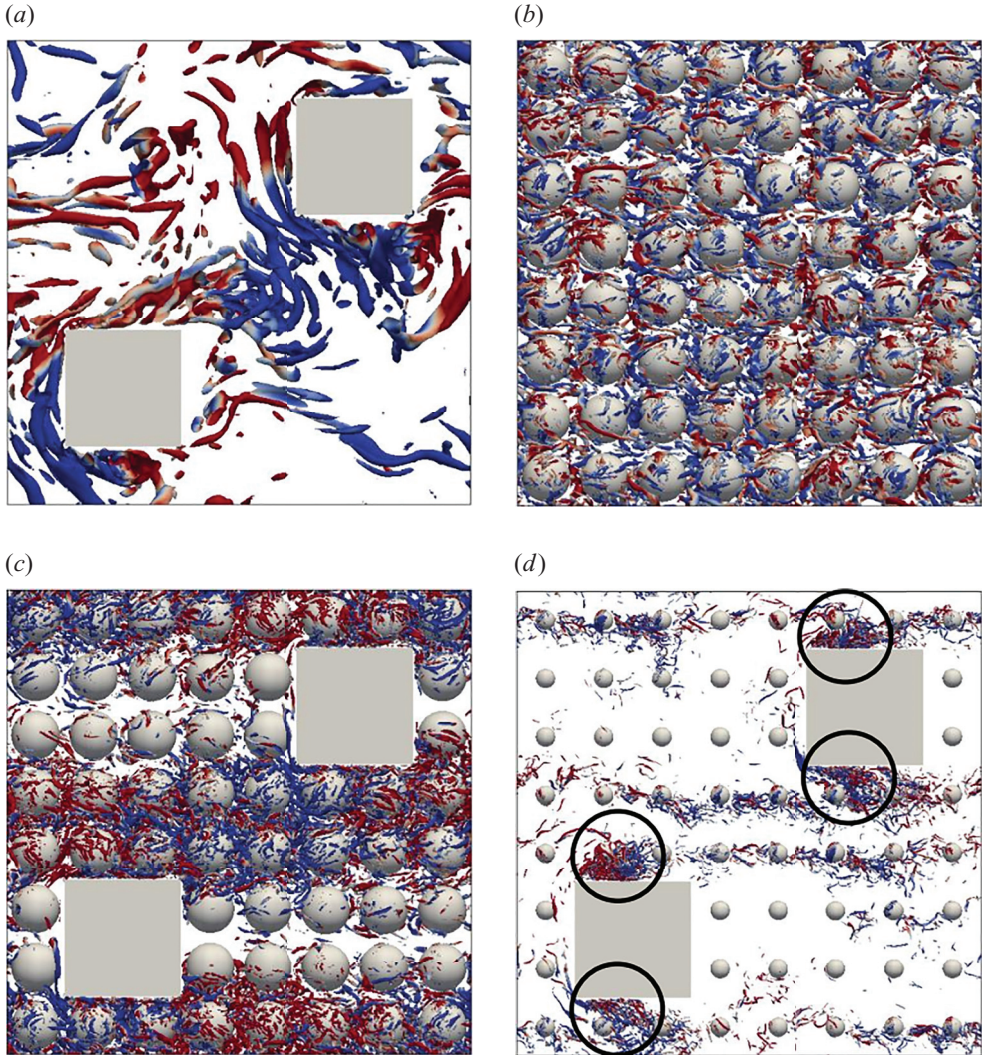
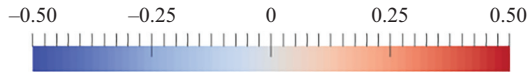


Figure 2. Instantaneous turbulence structures, colour coding showing the instantaneous value of the vertical velocity u_2 , $Q/Q_M = 2 \times 10^{-2}$, where Q_M is the maximum value of Q . Possible large-scale structures are indicated by circles. (a) Bars, $\phi_s = 1.0$, $Re_l = 641$, $Q_M d_l^2 / u_m^2 = 4.8 \times 10^3$; (b) spheres, $\phi_s = 0.70$, $Re_s = 545$, $Re_l = 1308$, $Q_M d_l^2 / u_m^2 = 2.0 \times 10^4$; (c) bars and spheres, $\phi_s = 0.70$, $Re_s = 536$, $Re_l = 1286$, $Q_M d_l^2 / u_m^2 = 1.4 \times 10^4$; (d) bars and spheres, $\phi_s = 0.98$, $Re_s = 564$, $Re_l = 3384$, $Q_M d_l^2 / u_m^2 = 2.0 \times 10^5$.

It can be seen that, if the porous matrix has only large porous elements ('bars'), \hat{R}_{11} is non-zero as the distance from the centre point $x_1 - x_{10}$ is in the range $[-s_l, s_l]$, while \hat{R}_{22} is non-zero as $x_2 - x_{20}$ is in the range $[-s_l, s_l]$, indicating that the turbulence close to the domain centre has the length scale s_l , see the dash-dotted lines in figure 3. If the porous matrix has also small porous elements ('spheres') with a medium porosity ($\phi_s = 0.7$), no matter the large porous elements ('bars') exist or not, the non-zero ranges of \hat{R}_{11} and

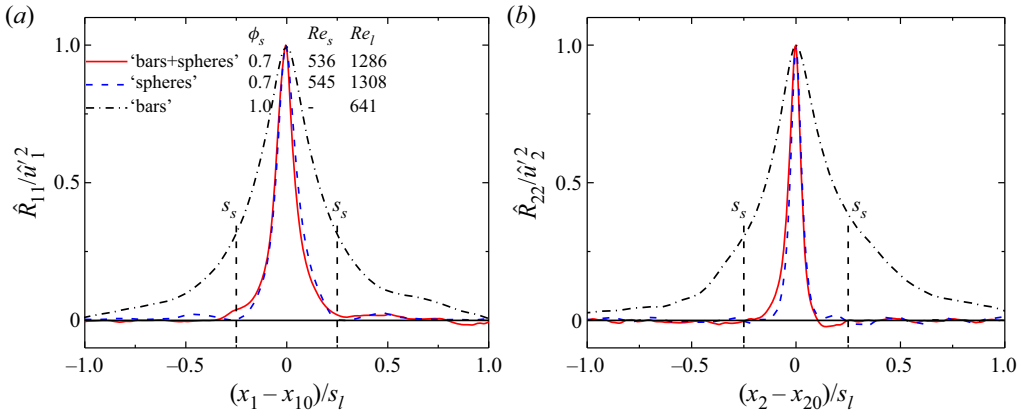


Figure 3. Turbulent two-point correlations in the streamwise (x_1) direction (a) and transverse (x_2) direction (b).

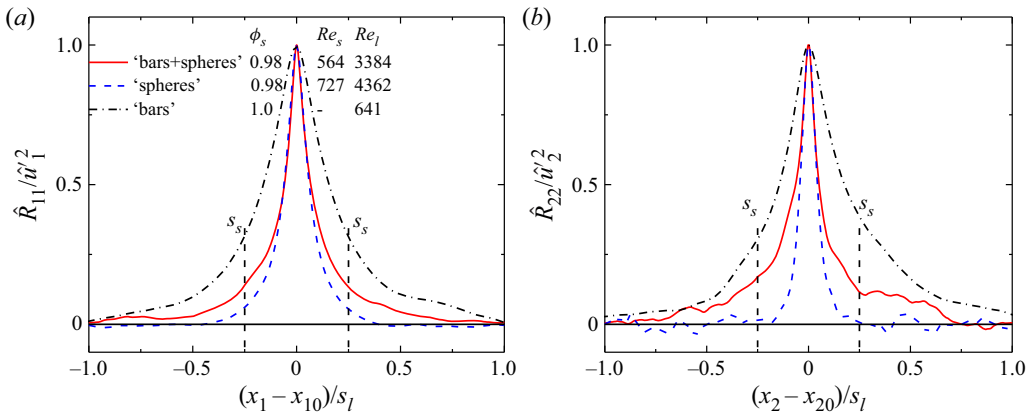


Figure 4. Turbulent two-point correlations in the streamwise (x_1) direction (a) and transverse (x_2) direction (b).

\hat{R}_{22} are reduced to $[-\frac{1}{4}s_l, \frac{1}{4}s_l]$, see the solid and dashed lines in figure 3. The turbulence has the length scale $\frac{1}{4}s_l$ which is identical to the small pore size $s_s = \frac{1}{4}s_l$. The DNS results confirm the PSPH, which states that, for a porous matrix with medium to low porosity, the turbulence length scale is generally determined by the pore size and there is no macroscopic turbulence.

As the value of ϕ_s is increased to 0.98 while the Reynolds number is kept high enough to ensure the flow to be fully turbulent, the non-zero ranges of \hat{R}_{11} and \hat{R}_{22} for 'bars+spheres' become wider than $[-\frac{1}{4}s_l, \frac{1}{4}s_l]$, see figure 4. They are also larger than the non-zero ranges for 'spheres'. The DNS results indicate that macroscopic turbulence survives in this condition.

The integral length scales can be calculated from the turbulent two-point correlations to quantify the length scale of turbulence. Similar to the definitions in Pope (2000), the longitudinal integral length scales in the parallel (x_1) and transverse (x_2) directions L_x and L_y are, respectively, calculated as

$$L_x = \int_{-s_l}^{s_l} \hat{R}_{11}(r_1 \mathbf{e}_1, \mathbf{x}_0) / \hat{u}_1^2(\mathbf{x}_0) dr_1, \quad (4.4)$$

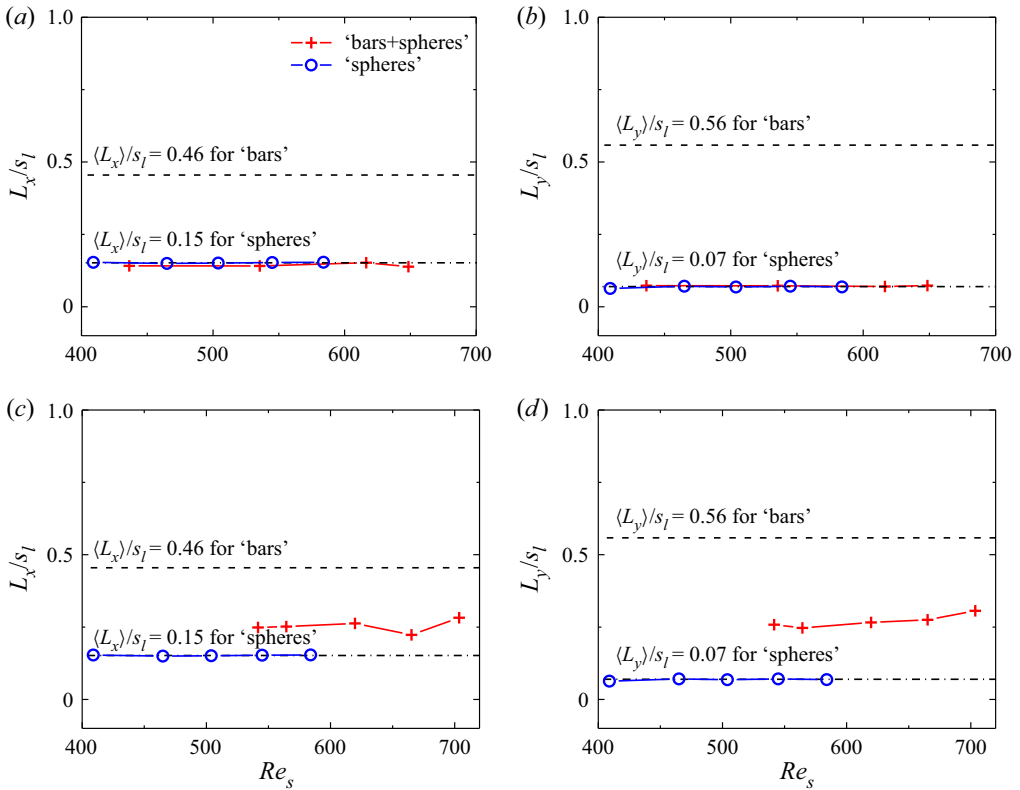


Figure 5. Effects of the Reynolds number on the integral length scales: (a) L_x/s_I , $\phi_s = 0.70$; (b) L_y/s_I , $\phi_s = 0.70$; (c) L_x/s_I , $\phi_s = 0.98$; (d) L_y/s_I , $\phi_s = 0.98$.

$$L_y = \int_{-s_I}^{s_I} \hat{R}_{22}(r_2 \mathbf{e}_2, \mathbf{x}_0) / \hat{u}_2^2(\mathbf{x}_0) dr_2, \quad (4.5)$$

where L_x and L_y for 'bars+spheres' with different Reynolds numbers Re_s are shown in figure 5. They are compared with the integral length scales in the porous matrices with only large length scale ('bars') or small length scale ('spheres'). Here L_x and L_y are averaged in a certain range of Reynolds numbers ($Re_s \in [400, 600]$ for 'spheres' and $Re_s \in [528, 653]$ for 'bars') for further analysis. The averaged integral length scales $\langle L_x \rangle/s_I$ and $\langle L_y \rangle/s_I$ for 'spheres' are 0.15 and 0.07, respectively. They are much lower than the averaged integral length scales for 'bars', which are 0.46 and 0.56, respectively. It can be seen in figures 5(a) and 5(b) that the L_x/s_I and L_y/s_I values for 'bars+spheres' change only marginally with the Reynolds number Re_s or Re_I . They are close to the values for 'spheres'; this implies that the macroscopic turbulence cannot be stimulated by increasing the Reynolds number. By contrast, L_x/s_I and L_y/s_I become closer to the values for 'bars' as the porosity ϕ_s is increased to 0.98, suggesting that the macroscopic turbulence occurs in this condition, see figures 5(c) and 5(d).

Figure 6 shows the averaged integral length scales $\langle L_x \rangle/s_I$ and $\langle L_y \rangle/s_I$ for $\phi_s = 0.7$ and the pore-scale ratio s_I/s_s in the range 4–12. The difference between the length scale of macroscopic turbulence and the pore-scale turbulence becomes more evident as the scale ratio s_I/s_s becomes larger. As s_I/s_s is increased from 4 to 12, $\langle L_x \rangle/s_I$ is decreased from 0.14 to 0.05, while $\langle L_y \rangle/s_I$ is decreased from 0.07 to 0.02. They are almost identical to the

Survival of macroscopic turbulence in porous media

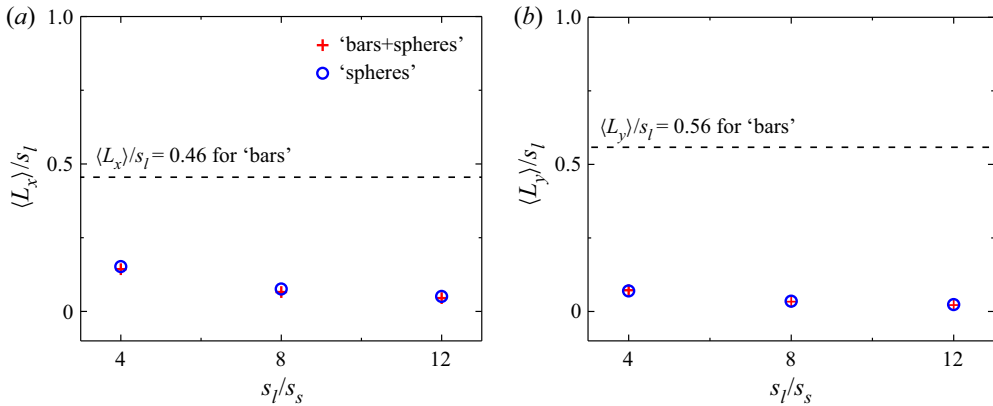


Figure 6. Effects of s_l/s_s on the averaged integral length scales, $\phi_s = 0.70$. The length scales are averaged in the range $Re_s \in [436, 649]$ with (a) $\langle L_x \rangle / s_l$; (b) $\langle L_y \rangle / s_l$.

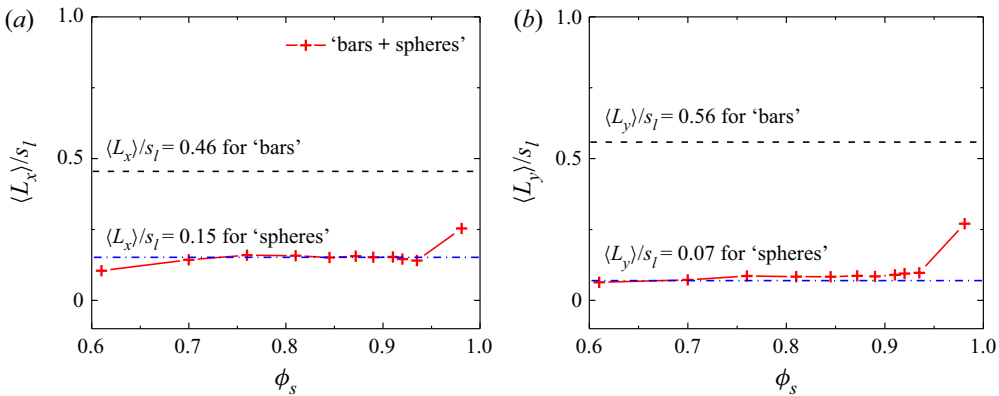


Figure 7. Effects of the porosity ϕ_s on the averaged integral length scales with (a) $\langle L_x \rangle / s_l$; (b) $\langle L_y \rangle / s_l$.

integral length values when the porous matrix has only small porous elements (spheres). The DNS results confirm that there is no macroscopic turbulence for this porosity value.

Figure 7 shows the relationship between the integral length scales and the porosity ϕ_s when the flow is fully turbulent. The DNS results for ‘bars+spheres’ are compared with those for ‘bars’ and ‘spheres’. Here $\langle L_x \rangle / s_l$ and $\langle L_x \rangle / s_l$ change only marginally as ϕ_s is increased from 0.61 to 0.93, while an abrupt jump can be found for $\phi_s = 0.98$, which indicates the onset of macroscopic turbulence. So, we expect that the critical porosity ϕ_c for the survival of macroscopic turbulence lies between 0.93 and 0.98. It should be noted that, up to now, this critical porosity value is only validated for the scale ratio $s_l/s_s = 4$.

Another porous matrix has been studied to understand the effects of pore-scale geometry on the critical porosity ϕ_c . The small porous elements for this porous matrix are made of cubes. Figure 8 shows the averaged integral length scales for different porous matrices. It can be seen that the values of $\langle L_x \rangle / s_l$ and $\langle L_y \rangle / s_l$ for ‘bars+cubes’ are close to the values for ‘cubes’ as ϕ_s is increased from 0.86 to 0.96. They jump abruptly and become close to the values for ‘bars’ as ϕ_s is increased to 0.98. The DNS results suggest that the critical value for the onset of macroscopic turbulence lies between 0.96 and 0.98. Again, this critical porosity is only validated for the scale ratio $s_l/s_s = 4$.

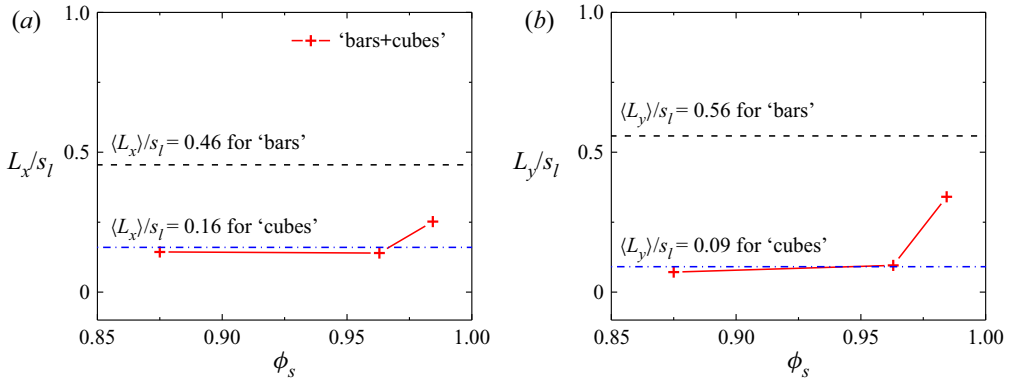


Figure 8. The averaged integral length scales for ‘bars+cubes’ with (a) $\langle L_x \rangle / s_l$; (b) $\langle L_y \rangle / s_l$.

The one-dimensional energy spectra at the domain centre can be calculated using the DNS results for two-point correlations. According to the definition by Kolmogorov (1941) for locally homogeneous and isotropic turbulence, it is calculated as

$$\hat{E}_{ii}(\mathbf{x}_0, k_1) = \frac{1}{\pi} \int_{-\infty}^{\infty} \hat{R}_{ii}(x_1 \mathbf{e}_1, \mathbf{x}_0) \exp(-ik_1 x_1) dx_1, \quad (4.6)$$

where k_1 denotes the wavenumber in the x_1 direction. Jin *et al.* (2015) and Gomes-Fernandes, Ganapathisubramani & Vassilicos (2015) argued that this equation can be also used to calculate the local energy spectra for inhomogeneous and anisotropic flows.

Figure 9 shows the premultiplied energy spectra $k_1 \hat{E}_{ii}(\mathbf{x}_0, k_1)$, which can be used to identify the k_1^{-1} range (Jimenez 1998). The Reynolds numbers are high enough to ensure the flow is fully turbulent. The maximum of wavelength $\Lambda = 2\pi/k_1$ which corresponds to the peak values of $k_1 \hat{E}_{ii}(\mathbf{x}_0, k_1)$ represents the largest length scale of turbulent structures (Guala, Hommema & Adrian 2006; Balakumar & Adrian 2007). When the porous matrix has only large porous elements (bars), the maximum value of Λ is approximately $5.3s_s$, which is between $s_l = 4s_s$ and $2s_l = 8s_s$, while it is much larger than the small pore scale s_s . When the porosity for the small porous elements has a medium value ($\phi_s = 0.7$), no matter the porous matrix has one (‘spheres’) or two (‘bars+spheres’) length scales, the maximum value of Λ is approximately $1.6s_s$, which is close to the small pore scale s_s . By contrast, when the porous matrix has two length scales (‘bars+spheres’) and the porosity is large ($\phi_s = 0.98$), the second peak of $k_1 \hat{E}_{ii}(\mathbf{x}_0, k_1)$ can be observed. The corresponding value of Λ is approximately $4s_s$, which is close to the maximum Λ for ‘bars’. The premultiplied energy spectra also confirm the occurrence of macroscopic turbulence at $\phi_s = 0.98$.

4.3. Macroscopic simulation results

The DNS results show that, when the Reynolds number is high enough to ensure the flow become fully turbulent, the porosity has a critical value ϕ_c for the occurrence of macroscopic turbulence. Now ϕ_c is generally independent of the Reynolds number and the shape of porous elements. However, it might be affected by the Darcy number which is determined by the scale ratio s_l/s_s . To further investigate the generality of ϕ_c , we have calculated the turbulent flows in the same porous matrices using macroscopic simulation.

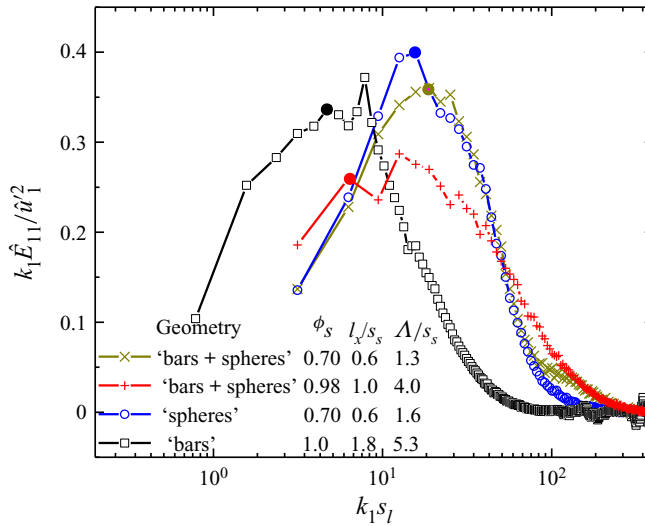


Figure 9. Premultiplied energy spectra for ‘bars+spheres’, ‘bars’ and ‘spheres’, $s_l/s_s = 4$. The peaks with the lowest wave-numbers are indicated with solid circles. The values of Re_s are 536 for ‘bars+spheres’ with $\phi_s = 0.7$, 564 for ‘bars+spheres’ with $\phi_s = 0.98$ and 545 for ‘spheres’, respectively. The value of Re_l for ‘bars’ is 641.

The instantaneous velocity magnitude in a cross-section for different values of porosity ϕ_s is shown in figure 10. The Reynolds number Re_l is 5060 for $\phi_s = 0.93$, which is much higher than the critical value of Re_l for the onset of macroscopic turbulence when the porous matrix has only large porous elements. The value of Re_K is 1302, suggesting that the flow is in the Forchheimer regime. However, no macroscopic turbulence is found in this case, see figure 10(a), while the microscopic turbulence is modelled. The macroscopic turbulence survives as the porosity ϕ_s is increased to 0.98 (figure 10b). Similarly, macroscopic turbulence is also found as ϕ_s is further increased, see figure 10(c) for $\phi_s = 0.99$ and figure 10(d) for $\phi_s = 1$. The macroscopic simulation results are consistent with the DNS results.

Figure 11 shows the turbulent two-point correlation $\hat{R}_{11}(r, x_0)$ calculated from the macroscopic simulation. The test cases have similar values of Re_K . Now $\hat{R}_{11}(r, x_0)$ is equal to zero when $\phi_s = 0.93$ but has a non-zero range when $\phi_s \geq 0.98$. This non-zero range of $\hat{R}_{11}(r, x_0)$ exceeds $[-\frac{1}{4}s_l, \frac{1}{4}s_l]$, which corresponds to the microscopic length scale, and becomes wider as ϕ_s is increased from 0.98 to 1.

Figure 12 shows the relationship between the Reynolds number Re_K and the normalized macroscopic turbulence kinetic energy $2\langle k \rangle / u_m^2$ for $\phi_s = 0.98$ and different Da values. The onset of macroscopic turbulence occurs at $Re_K = 133$ for $Da = 0.39$ or $Re_K = 120$ for $Da = 0.10$. The results are consistent with the statement by Nield & Bejan (2017) that the transition from a Darcy flow to a Darcy–Forchheimer flow occurs when Re_K is of order 10^2 . In addition, we have found that the values of $2\langle k \rangle / u_m^2$ change only marginally when the Re_K is above 1000.

The longitudinal integral length scales L_x and L_y for $Re_K > 1000$ are shown in figure 13. The macroscopic results are compared with the DNS results for ‘bars’. Both macroscopic simulation and DNS results show that L_x and L_y change only marginally when the value of Re_K is increased. The values of L_x and L_y increase with the increase of ϕ_s and approach the values for $\phi_s = 1$. The macroscopic simulation results of $\langle L_x \rangle$ and $\langle L_y \rangle$ for $\phi_s = 1$ are 0.45 and 0.54, respectively, which are close to DNS results for ‘bars’.

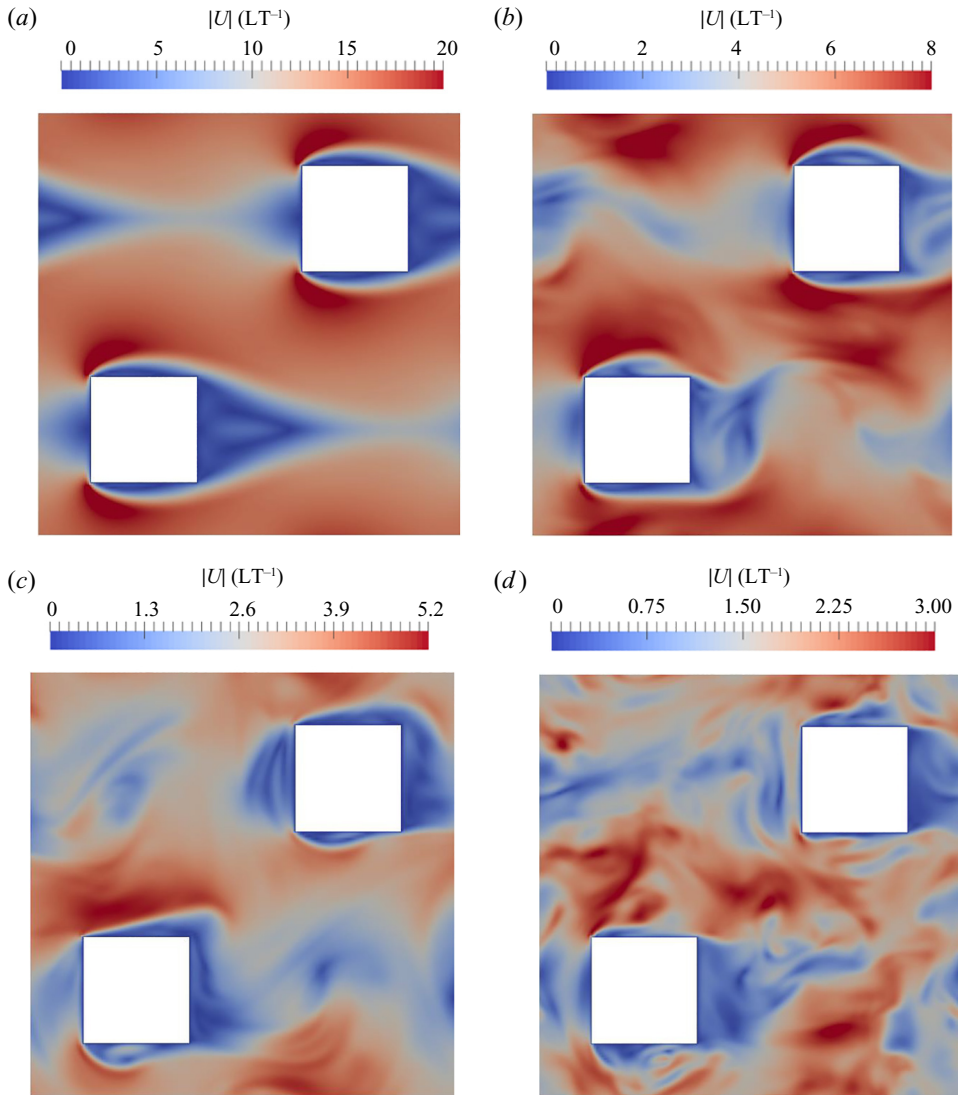


Figure 10. Instantaneous velocity magnitude, ‘bars+spheres’ with (a) $\phi_s = 0.93$, $Da = 0.07$, $Re_K = 1302$, $Re_l = 5060$; (b) $\phi_s = 0.98$, $Da = 0.39$, $Re_K = 1225$, $Re_l = 1969$; (c) $\phi_s = 0.99$, $Da = 1.26$, $Re_K = 1135$, $Re_l = 1009$; (d) $\phi_s = 1.0$, $Re_l = 630$.

Figure 14 shows the premultiplied energy spectra of macroscopic simulation results. A plateau of $k_1 \hat{E}_{11} / u_1^2 \approx 0.35$ can be found for porosity $\phi_s = 1$, which indicates the range of large-scale turbulent motion. The peak of $k_1 \hat{E}_{11}$ for $\phi_s = 1$ corresponds to the wavelength $\Lambda = 1.33s_l$, which is identical to the value of Λ for $\phi_s = 0.99$. When the porosity ϕ_s is decreased to 0.98, the value of Λ declines to s_l which is identical to the large pore size.

The macroscopic simulation results discussed above are for a GPM made of spherical porous elements with the scale ratio $s_l/s_s = 4$ or 8. The permeability K is calculated using the Carman–Kozeny equation (3.10). However, the values of K and the Darcy numbers calculated from this equation might have uncertainties due to the variation of the pore-scale geometries. To better understand the dependence of the critical porosity ϕ_c on

Survival of macroscopic turbulence in porous media

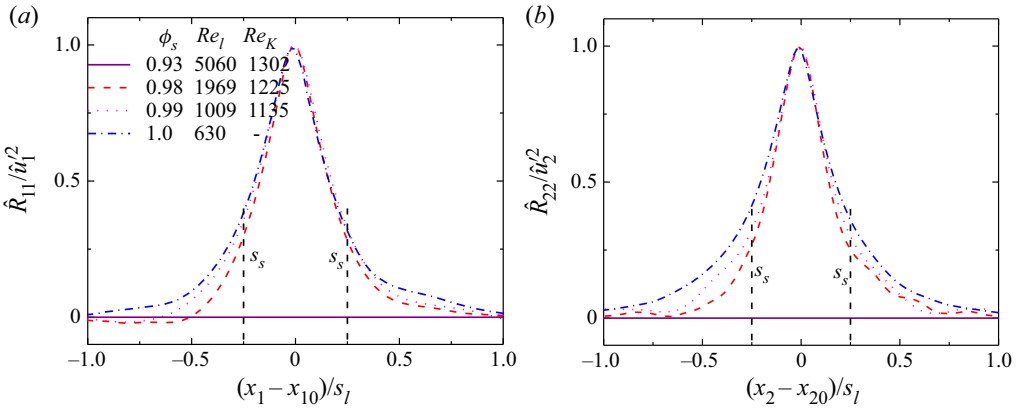


Figure 11. Turbulent two-point correlations in the streamwise (x_1) direction (a) and transverse (x_2) direction (b), ‘bars+spheres’.

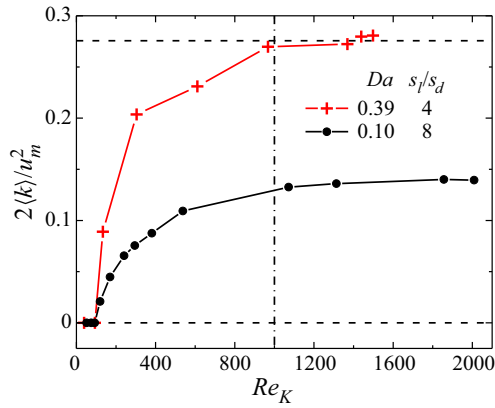


Figure 12. Normalized macroscopic turbulence kinetic energy $2\langle k \rangle / u_m^2$ versus Reynolds number Re_K , $\phi_s = 0.98$, ‘bars+spheres’.

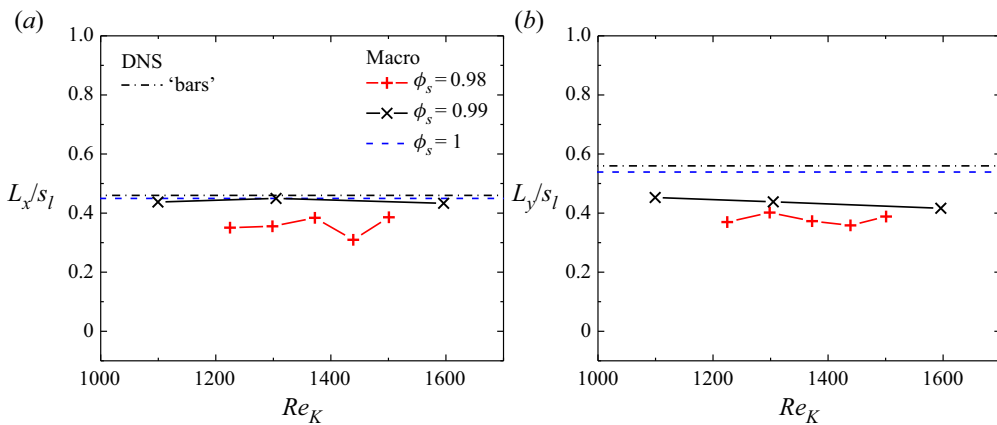


Figure 13. Turbulent two-point correlations in the streamwise (x_1) direction and transverse (x_2) direction, ‘bars+spheres’ with (a) L_x ; (b) L_y .

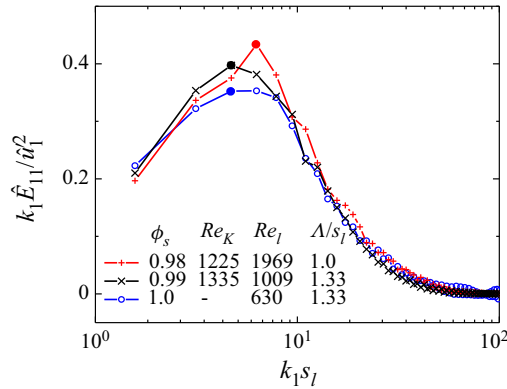


Figure 14. Premultiplied energy spectra for ‘bars+spheres’. The peaks with the lowest wavenumbers are indicated with solid circles.

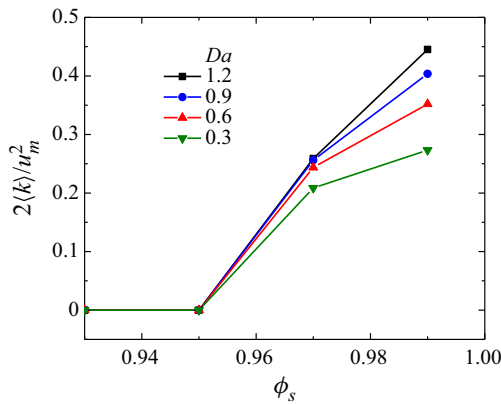


Figure 15. Normalized macroscopic turbulence kinetic energy $2\langle k \rangle / u_m^2$ versus porosity. Here $Re_l \rightarrow \infty$, $Da \in [0.3, 1.2]$, ‘bars+GPM’.

the Darcy number, we have solved (3.13) and (3.14) with the drag terms expressed by (3.17) and (3.18) for different Darcy numbers. The solutions are independent of the Reynolds numbers. Figure 15 shows the relationship between ϕ_s and $2\langle k \rangle / u_m^2$. The macroscopic simulation results indicate that the critical porosity ϕ_c for the survival of macroscopic turbulence is between 0.95 and 0.97, which is similar to the DNS results. Now ϕ_c is not sensitive to the Darcy number when it is in the range 0.3–1.2. When ϕ_s is smaller than ϕ_c , macroscopic turbulence cannot be stimulated even if $Re_l \rightarrow \infty$.

5. Conclusions

In order to understand whether macroscopic turbulence might survive in certain conditions and thus know the valid domain of the PSPH, we have studied the turbulent flows in porous matrices which have one or two length scales using DNS and macroscopic simulation. The large porous elements are made of two-dimensional bars with the element size d_l and spacing s_l , while the small porous elements are made of spheres or cubes with the element size d_s and spacing s_s .

Instantaneous Q isosurfaces, turbulent two-point correlations, integral length scales and premultiplied energy spectra which are obtained from both DNS and macroscopic

Test cases	ϕ_s	Mesh resolution	Accuracy		
			Re_s	Re_l	Δ (%)
'bars+spheres'	0.89	$545 \times 545 \times 273$	571	1941	8.0
	0.91	$577 \times 577 \times 289$	600	2160	6.3
	0.92	$609 \times 609 \times 305$	636	2417	5.6
	0.93	$641 \times 641 \times 321$	615	2460	5.1
	0.98	$961 \times 961 \times 481$	704	4224	1.0
'bars+cubes'	0.88	$641 \times 641 \times 321$	628	2512	7.3
	0.96	$961 \times 961 \times 481$	614	3684	1.3
	0.98	$1281 \times 1281 \times 641$	749	5992	0.2
'spheres'	0.70	$385 \times 385 \times 193$	465	1116	6.0
	0.76	$417 \times 417 \times 209$	476	1238	2.7
	0.81	$449 \times 449 \times 225$	647	1812	4.0
	0.84	$481 \times 481 \times 241$	623	1869	1.0
	0.87	$513 \times 513 \times 257$	775	2480	3.0
'bars'	—	$161 \times 161 \times 161$	—	528	3.0
	—	$161 \times 161 \times 161$	—	594	6.8
	—	$161 \times 161 \times 161$	—	630	7.9
	—	$161 \times 161 \times 161$	—	641	8.6
	—	$161 \times 161 \times 161$	—	653	8.5

Table 3. Main parameters for the typical DNS cases, LBM.

simulation are used to detect the possible macroscopic turbulence. The DNS results show that the critical porosity ϕ_c for the survival of macroscopic turbulence is between 0.93 and 0.98 when the scale ratio s_l/s_s is set to 4. When the porosity is lower than ϕ_c , the integral length scales for porous matrices with two length scales ('bars+spheres' or 'bars+cubes') are almost identical to those for porous matrices with only small porous elements ('spheres' or 'cubes'). When the flow is fully turbulent, the value of ϕ_c does not change markedly as the Reynolds number (Re_s or Re_l) is increased or the pore-scale elements are changed from 'spheres' to 'cubes'.

The generality of the value of ϕ_c is further studied using macroscopic simulation. The porous matrix made of spherical elements is modelled as a continuous porous medium whose geometric parameters are determined empirically. The macroscopic simulation results for 'bars+spheres' show that ϕ_c is in the range 0.95–0.97, which is close to the DNS results. Then, the macroscopic simulations for $Re_l \rightarrow \infty$ and the Darcy number values in the range 0.3–1.2 are performed. The numerical results show that ϕ_c is still in the range 0.95–0.97. It should be noted that that c_{B2} for our macroscopic simulation is calculated using (3.12) and the coefficient of the Forchheimer term is set to $c_{F1} = 0.1$. The current critical porosity value ϕ_c is calculated based on the coefficient c_{B2} and c_{F1} values. When the Darcy number approaches zero, the macroscopic turbulence might survive only with larger critical porosity since the drag term becomes infinity in (3.17). The effect of pore-scale geometries on these coefficients has not been taken into account in our study. In addition, the DNS is for only two pore-scale geometries ('spheres' and 'cubes'). The dependence of the critical porosity on the pore-scale geometry still needs to be further investigated.

The comparison between the DNS and macroscopic simulation results also confirms the accuracy of the PSPH model proposed by Rao *et al.* (2020), as well as the capability of using this model to directly resolve the macroscopic turbulence in porous media.

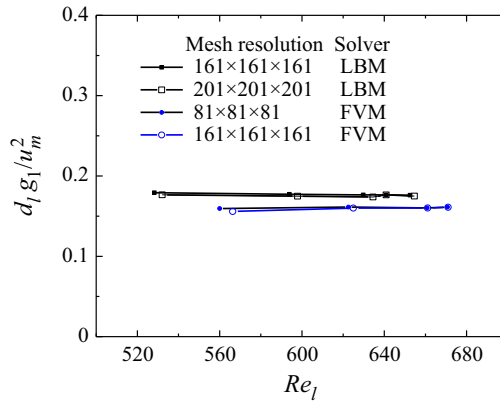


Figure 16. Applied pressure gradient g_1 versus Reynolds number Re_l , DNS results. The porous matrix is made of staggered arrays of bars. Here FVM and LBM results with different mesh resolutions are compared.

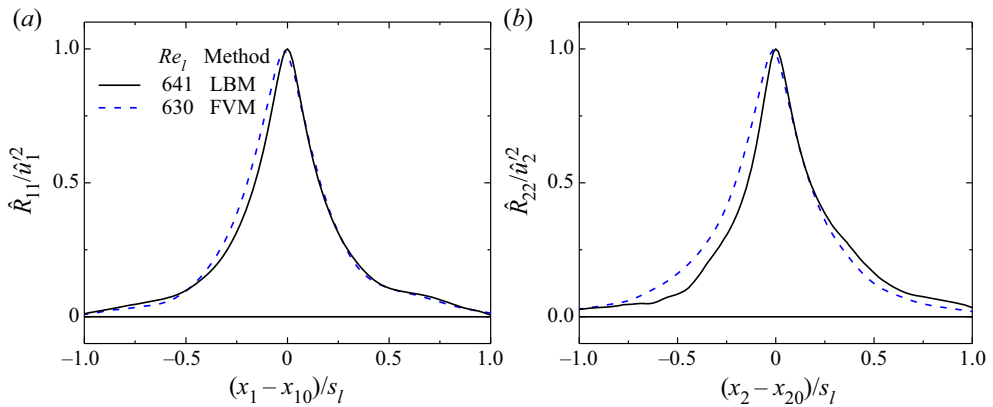


Figure 17. Turbulent two-point correlations in the streamwise (x_1) direction (a) and transverse (x_2) direction (b). The porous matrix is made of staggered arrays of bars. Here FVM and LBM results are compared.

Acknowledgements. The authors gratefully acknowledged the support of this study by China Scholarship Council (CSC). Acknowledgment is also given to Professor M. Avila for the illuminating discussion with him. All parallel computations are performed using the cluster of the Center of Applied Space Technology and Microgravity (ZARM), University of Bremen.

Declaration of interests. The authors report no conflict of interest.

Author ORCIDs.

Feixiong Rao <http://orcid.org/0000-0002-7338-7969>;

Yan Jin <http://orcid.org/0000-0002-2297-6827>.

Appendix A. Verification and validation

The accuracy of the DNS solution can be examined by an accuracy measure, which we define as

$$\Delta = \frac{g_1 - g_s}{g_1}, \tag{A1}$$

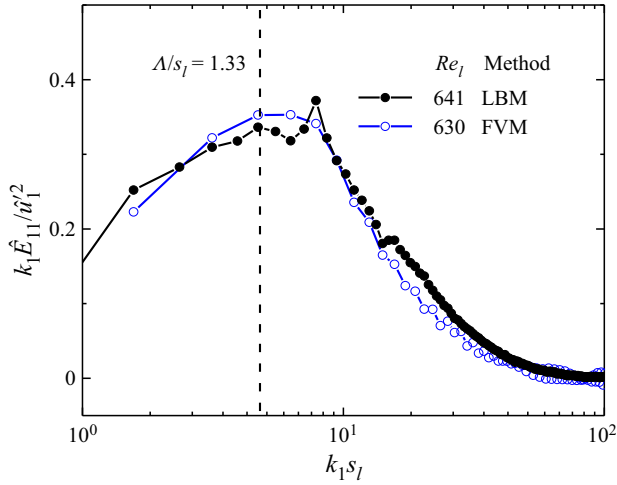


Figure 18. Premultiplied energy spectra. The porous matrix is made of staggered arrays of bars. Here FVM and LBM results are compared.

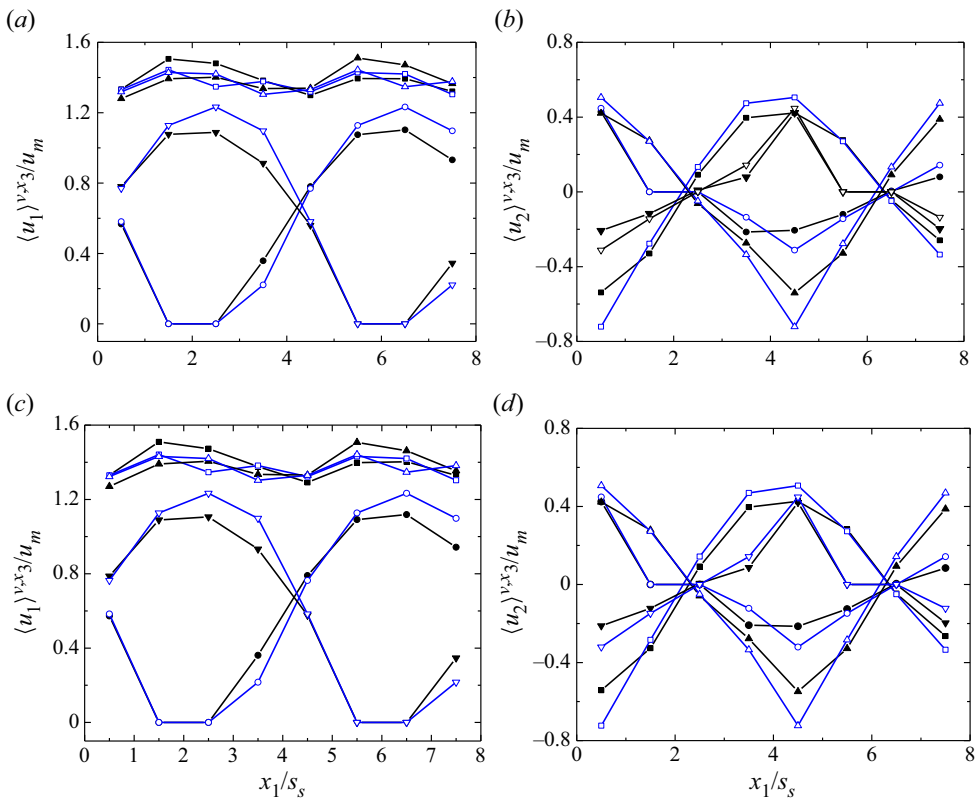


Figure 19. Distribution of $\langle \bar{u}_1 \rangle^{v,x_3}$ and $\langle \bar{u}_2 \rangle^{v,x_3}$ along the streamwise (x_1) lines at $x_2/s_s = 0.5$ (squares), 2.5 (circles), 4.5 (up-pointing triangles) and 6.5 (down-pointing triangles). Solid symbols indicate DNS results and hollow symbols indicate macroscopic simulation results. The porous matrix is ‘bars+spheres’ with $\phi_s = 0.70$. The Reynolds number Re_s is 436 (a,b) or 620 (c,d).

where g_1 and g_s are the pressure gradient in the streamwise direction and the volume-averaged dissipation rate in the computational domain. Jin *et al.* (2015) suggested that a solution with Δ values below 10% for this type of flows is accurate enough for the analysis. Table 3 shows the values of Δ for typical DNS cases.

The FVM and LBM methods have been intensively applied and verified in our previous studies, see Jin *et al.* (2015), Uth *et al.* (2016), Jin & Kuznetsov (2017) and Rao *et al.* (2020). Here we make further verification using the cases in this study. Figure 16 shows the relationship between Re_l and the drag coefficient $f_D = d_l g_1 / u_m^2$ calculated from different mesh resolutions and solvers (the FVM and the LBM). The porous matrix is made of staggered arrays of bars. It can be seen that calculated Re_l is only marginally changed as the number of mesh cells is increased. The LBM results for the applied pressure gradient are approximately 6% higher than the FVM results. The reason is that the bounced back model used in the LBM leads to slightly larger solid region; this is an acknowledged error. Figures 17 and 18 show the LBM and FVM results for the two-point correlations and the premultiplied energy spectra; the marginal difference does not affect our analysis.

The cases ‘bars+spheres’ with $\phi_s = 0.70$ are calculated using both DNS and macroscopic simulation methods. Figure 19 shows the time-, REV- and spanwise (x_3) averaged velocity components $\langle \bar{u}_1 \rangle^{v,x_3}$ and $\langle \bar{u}_2 \rangle^{v,x_3}$ along the streamwise (x_1) lines. It can be seen that the macroscopic simulation results are in reasonable accordance with the DNS results; the macroscopic simulation model is well validated.

REFERENCES

- AIDUN, C.K. & CLAUSEN, J.R. 2009 Lattice-Boltzmann method for complex flows. *Annu. Rev. Fluid Mech.* **41**, 439–472.
- ANTOHE, B.V. & LAGE, J.L. 1997 A general two-equation macroscopic turbulence model for incompressible flow in porous media. *Intl J. Heat Mass Transfer* **40**, 3013–3024.
- BALAKUMAR, B.J. & ADRIAN, R.J. 2007 Large- and very-large-scale motions in channel and boundary-layer flows. *Phil. Trans. R. Soc. Lond. A* **365**, 665–681.
- BELCHER, S.E., HARMAN, I.N. & FINNIGAN, J.F. 2012 The wind in the willows: flows in forest canopies in complex terrain. *Annu. Rev. Fluid Mech.* **44**, 479–504.
- BHATNAGAR, P.L., GROSS, E.P. & KROOK, M. 1954 A model for collision processes in gases. I. Small amplitude processes in charged and neutral one-component systems. *Phys. Rev.* **94**, 511–525.
- BREUGEM, W.P., BOERSMA, B.J. & UITTENBOGAARD, R.E. 2006 The influence of wall permeability on turbulent channel flow. *J. Fluid Mech.* **562**, 35–72.
- CARMAN, P.C. 1956 *Flow of Gases Through Porous Media*. Academic Press.
- CHEN, S. & DOOLEN, G.D. 1998 Lattice Boltzmann method for fluid flows. *Annu. Rev. Fluid Mech.* **30**, 329–364.
- CHU, X., WEIGAND, B. & VAIKUNTANATHAN, V. 2018 Flow turbulence topology in regular porous media: from macroscopic to microscopic scale with direct numerical simulation. *Phys. Fluids* **30**, 065102.
- DE LANGRE, E. 2008 Effects of wind on plants. *Annu. Rev. Fluid Mech.* **40**, 141–168.
- DE LEMOS, M.J.S. 2012 *Turbulence in Porous Media: Modeling and Applications*, 2nd edn. Elsevier.
- GETACHEW, D., MINKOWYCY, W.J. & LAGE, J.L. 2000 A modified form of the model for turbulent flows of an incompressible fluid in porous media. *Intl J. Heat Mass Transfer* **43**, 2909–2915.
- GHISALBERTI, M. & NEPF, H. 2009 Shallow flows over a permeable medium: the hydrodynamics of submerged aquatic canopies. *Trans. Porous Med.* **78**, 309.
- GOMES-FERNANDES, R., GANAPATHISUBRAMANI, B. & VASSILICOS, J.C. 2015 The energy cascade in near-field non-homogeneous non-isotropic turbulence. *J. Fluid Mech.* **771**, 676–705.
- GRAY, W.G. & LEE, P.C.Y. 1977 On the theorems for local volume averaging of multiphase systems. *Intl J. Multiphase Flow* **3**, 333–340.
- GUALA, M., HOMMEMA, S.E. & ADRIAN, R.J. 2006 Large-scale and very-large-scale motions in turbulent pipe flow. *J. Fluid Mech.* **554**, 521–542.
- HUNT, J.C.R., WARY, A.A. & MOIN, P. 1988 Eddies, stream, and convergence zones in turbulent flows. *Center for Turbulence Research Report CTR-S88*, pp. 193–208.

Survival of macroscopic turbulence in porous media

- JIMENEZ, J. 1998 The largest scales of turbulent wall flows. In *Center for Turbulence Research, Annual Research Briefs*, pp. 137–154. Stanford University.
- JIN, Y. & KUZNETSOV, A.V. 2017 Turbulence modeling for flows in wall bounded porous media: qan analysis based on direct numerical simulations. *Phys. Fluids* **29**, 045102.
- JIN, Y., UTH, M.-F., KUZNETSOV, A.V. & HERWIG, H. 2015 Numerical investigation of the possibility of macroscopic turbulence in porous media: A direct numerical simulation study. *J. Fluid Mech.* **766**, 76–103.
- KAZEROONI, R.B. & HANNANI, S.K. 2009 Simulation of turbulent flow through porous media employing a $v2f$ model. *Sci. Iran. Trans. B* **16**, 159–167.
- KIM, T., BLOIS, G., BEST, J.L. & CHRISTENSEN, K.T. 2020 Experimental evidence of amplitude modulation in permeable-wall turbulence. *J. Fluid Mech.* **887**, A3.
- KOLMOGOROV, A.N. 1941 Dissipation of energy in locally isotropic turbulence. *Dokl. Akad. Nauk SSSR* **32**, 19–21.
- KOZENY, J. 1927 Ueber kapillare Leitung des Wassers im Boden. *Sitzb. Akad. Wiss. Wien. Math. naturw. Klasse.* **136**, 271–306.
- KUNDU, P., KUMAR, V. & MISHRA, I.M. 2014 Numerical modeling of turbulent flow through isotropic porous media. *Intl J. Heat Mass Transfer* **75**, 40–57.
- KUWAHARA, F., KAMEYAMA, Y., YAMASHITA, S. & NAKAYAMA, A. 1998 Numerical modeling of turbulent flow in porous media using a spatially periodic array. *J. Porous Media* **1**, 47–55.
- LAGE, J.L. & ANTOHE, B.V. 2000 Darcy's experiments and the deviation to nonlinear flow regime. *Trans. ASME J. Fluids Engng* **122**, 619–625.
- LEE, K.B. & HOWELL, J.R. 1991 Theoretical and experimental heat and mass transfer in highly porous media. *Intl J. Heat Mass Transfer* **34**, 2123–2132.
- MERONEY, R.N. 2007 Fires in porous media: natural and urban canopies. In *Flow and Transport Processes with Complex Obstructions* (ed. Y. A. Gayev & J. C. Hunt), vol. 236. Springer.
- MOHAMAD, A.A. 2011 *Lattice Boltzmann Method*. Springer.
- NAKAYAMA, A. & KUWAHARA, F. 1999 A macroscopic turbulence model for flow in a porous medium. *Trans. ASME J. Fluids Engng* **121**, 427–433.
- NEPF, H.M. 2012 Flow and transport in regions with aquatic vegetation. *Annu. Rev. Fluid Mech.* **44**, 123–142.
- NIELD, D.A. 1991 The limitations of the Brinkman-Forchheimer equation in modeling flow in a saturated porous medium and at an interface. *Intl J. Heat Fluid Flow* **12**, 269–272.
- NIELD, D.A. 2001 Alternative models of turbulence in a porous medium, and related matters. *Trans. ASME J. Fluids Engng* **123**, 928–931.
- NIELD, D.A. & BEJAN, A. 2017 *Convection in Porous media*, 5th edn. Springer.
- POPE, S.B. 2000 *Turbulent Flows*. Cambridge University Press.
- PRESCOTT, P.J. & INCROPERA, F.P. 1995 The effect of turbulence on solidification of a binary metal alloy with electromagnetic stirring. *Trans. ASME J. Heat Transfer* **117**, 716–724.
- RAO, F., KUZNETSOV, A.V. & JIN, Y. 2020 Numerical modeling of momentum dispersion in porous media based on the pore scale prevalence hypothesis. *Trans. Porous Med.* **133**, 271–292.
- RUBOL, S., LING, B. & BATTIATO, I. 2018 Universal scaling-law for flow resistance over canopies with complex morphology. *Sci. Rep.* **8**, 4430.
- SERRA, T., FERNANDO, H.J.S. & RODRIGUEZ, R. 2004 Effects of emergent vegetation on lateral diffusion in wetlands. *Water Res.* **38**, 139–47.
- SLATTERY, J.C. 1967 Flow of viscoelastic fluids through porous media. *AICHE J.* **13**, 1066–1071.
- SRIKANTH, V., HUANG, C.W., SU, T.S. & KUZNETSOV, A.V. 2018 Symmetry breaking in porous media as a consequence of the von Kármán instability. *Fluid Dyn.* [arXiv:1810.10141](https://arxiv.org/abs/1810.10141)
- SUGA, K. 2016 Understanding and modelling turbulence over and inside porous media. *Flow Turbul. Combust.* **96** (3), 717–756.
- TANINO, Y. & NEPF, H.M. 2008 Lateral dispersion in random cylinder arrays at high Reynolds number. *J. Fluid Mech.* **600**, 339–371.
- UTH, M.-F., JIN, Y., KUZNETSOV, A.V. & HERWIG, H. 2016 A direct numerical simulation study on the possibility of macroscopic turbulence in porous media: effects of different solid matrix geometries, solid boundaries, and two porosity scales. *Phys. Fluids* **28**, 065101.
- WHITAKER, S. 1969 Advances in theory of fluid motion in porous media. *Ind. Engng Chem.* **61**, 14–28.
- WHITAKER, S. 1999 *The Method of Volume Averaging*. Springer.